

Direct observation of excitonic instability in Ta₂NiSe₅

Kwangrae Kim,^{1,2,*} Hoon Kim,^{1,2,*} Jonghwan Kim,^{2,3} Changil Kwon,^{1,2} Jun Sung Kim,^{1,2} and B. J. Kim^{1,2,†}

¹*Department of Physics, Pohang University of Science and Technology, Pohang 37673, South Korea*

²*Center for Artificial Low Dimensional Electronic Systems,*

Institute for Basic Science (IBS), 77 Cheongam-Ro, Pohang 37673, South Korea

³*Department of Materials Science and Engineering,*

Pohang University of Science and Technology, Pohang 37673, Republic of Korea

(Dated: August 9, 2021)

I. ABSTRACT

Coulomb attraction between electrons and holes in a narrow-gap semiconductor or a semimetal is predicted to lead to an elusive phase of matter dubbed ‘excitonic insulator’. However, direct observation of such electronic instability remains extremely rare. Here, we report the observation of incipient divergence in the static excitonic susceptibility of the candidate material Ta₂NiSe₅ using Raman spectroscopy. Critical fluctuations of the excitonic order parameter give rise to quasi-elastic scattering of B_{2g} symmetry, whose intensity grows inversely with temperature toward the Weiss temperature of $T_W \approx 241$ K, which is arrested by a structural phase transition driven by an acoustic phonon of the same symmetry at $T_C = 325$ K. Concurrently, a B_{2g} optical phonon becomes heavily damped to the extent that its trace is almost invisible around T_C , which manifests a strong electron-phonon coupling that has obscured the identification of the low-temperature phase as an excitonic insulator for more than a decade. Our result unambiguously reveals the electronic origin of the phase transition.

II. INTRODUCTION

One of the most spectacular quantum phenomena is the formation of Bose-Einstein condensate (BEC), which allows quantum mechanical nature of the electron wave function to manifest as macroscopic observable properties. Prominent examples include superfluidity in atomic gases^{1,2} and the Josephson effect in superconductors^{3,4}. One such possibility is offered by excitons—bound pairs of electrons and holes—whose small mass and charge neutrality give rise to unique features in their condensed phase, such as vanishing Hall resistance^{5,6}. Indeed, exciton BEC has been observed in double quantum well systems, in which excitons can be generated optically⁷, electrically⁸, or magnetically through quantum Hall states^{5,6}.

However, realization of exciton BEC in thermal equilibrium turns out to be quite challenging and requires following materials design considerations^{9–12}: (i) The

density of electron-hole pairs has to be small enough for Coulomb interaction to be effective yet large enough to induce a condensation. This requires a fine tuning of the band gap; (ii) The valence and the conduction bands must have vanishing interband matrix element to avoid hybridization between them; (iii) The wave functions of the electrons and the holes should be spatially separated from each other to avoid their quick recombination into photons; (iv) Ideally, the bands should have a direct gap, positive (semiconductor) or negative (semimetal), to avoid unit cell enlargement.

Ta₂NiSe₅ is one of the few promising candidates, and, to our best knowledge, is the only one that has an instability at $\mathbf{q} = 0$ (refs. 13,14). Finite- \mathbf{q} instabilities, such as the one found in TiSe₂, result from an indirect gap¹⁵ and necessarily break the translational symmetry¹⁶. The latter is better known as a charge density wave insulator. Although the formation of charge density wave in TiSe₂ involves condensation of excitons¹⁷, an accompanying structural phase transition renders it difficult to distinguish it from a Peierls transition^{15–17}. The contrast between the two phases is analogous to the distinction between a Mott insulator and a Slater insulator: they become symmetry-wise indistinguishable when the unit cell is doubled by an antiferromagnetic order.

For a similar reason, it is difficult to differentiate the insulating phase of Ta₂NiSe₅ from a trivial band insulator^{18–38}. At its semimetal-to-insulator transition, Ta₂NiSe₅ undergoes a simultaneous structural phase transition^{39,40} from the high-temperature orthorhombic ($Cmcm$) phase to the low-temperature monoclinic ($C2/c$) phase (Fig. 1a). The group-subgroup relation between the two space groups implies a freezing of a B_{2g} phonon mode at the second-order phase transition. Indeed, softening of the B_{2g} acoustic mode, equivalent to the vanishing C_{55} elastic constant and consequent shearing of the Ta-Ni-Ta quasi-one-dimensional chain (Fig. 1a), has been observed by an inelastic x-ray scattering experiment³⁰. In the monoclinic phase, the valence band and the conduction band belong to the same irreducible representation (IR) along the Γ -Z direction, where they overlap with each other, thus allowing a band gap to open by a hybridization between them^{35,37}. Thus, as pointed out earlier^{14–17,20,23,24,26,33,37,38}, the distinction between an excitonic insulator and a band insulator in the presence of a lattice distortion may ultimately be only quantitative. However, if the transition is pri-

marily of electronic origin and the structural distortion is only a secondary effect, the latter may, in principle, be engineered away by a clever materials design. Thus, identification of the main driver of the transition is of fundamental importance and the first step toward realizing the elusive excitonic insulator.

III. RESULTS AND DISCUSSION

To address this issue, we monitor simultaneously the lattice and the electronic sectors across the transition using Raman spectroscopy, exploiting its unique access to symmetry-resolved electronic susceptibilities at the zone center. We start by analyzing Raman-active phonon modes. Ta_2NiSe_5 has twenty-four Raman-active optical phonon modes, which belong to either A_g or B_g IRs in the monoclinic $C2/c$ structure, and A_g , B_{1g} , B_{2g} , or B_{3g} IRs in the orthorhombic $Cmcm$ structure. In our experimental geometry (Fig. 1b), only the A_g modes (A_g and B_{2g}) are allowed in the monoclinic phase (orthorhombic phase) by Raman selection rules. Among the optical phonons, eleven of them are A_g modes in the low temperature phase ($C2/c$), which branch into three B_{2g} and eight A_g modes in the high temperature phase ($Cmcm$). Thus, the number of Raman-active phonon modes remains the same across the transition.

All of the eleven Raman-active phonons are clearly resolved at all measured temperatures from 120 K to 550 K. Figure 1c shows three representative unpolarized spectra: above, at, and below the transition. The highest-energy mode is found below 300 cm^{-1} , consistent with earlier works^{22,33,34,36}. The low temperature spectrum most clearly resolves all the phonon modes. Although they all formally belong to the A_g IR in the monoclinic phase, the ones that belong to the B_{2g} IR in the orthorhombic phase (mode 2, 5, and 6) have distinct patterns in their azimuth angle (Ψ : angle between incident light polarization and the a -axis) dependence (Fig. 1d, Supplementary Fig. 1 and Supplementary Table 1), consistent with the changes in the lattice structure being minor^{23,33}. Upon approaching T_C (Figs. 1c and 1e), mode 5 seemingly disappears in the unpolarized spectra, but it is well defined in the polarization-resolved spectrum measured at an azimuth angle that fully suppresses the A_g modes in the cross polarization (inset of Fig. 1c). Similarly, mode 2 displays an exceptionally strong damping, but is still visible at all temperatures. We note that these anomalies persist far above the T_C even outside of the temperature range in which the B_{2g} acoustic mode responsible for the structural transition shows significant softening³⁰. We will come back to discuss the temperature evolution of the phonon modes in more detail later on.

In addition to the strong phonon anomalies, we observe a remarkable upsurge of a quasi-elastic peak (QEP, marked by an inverted triangle in Fig. 1c) near the phase transition. Upon heating, the QEP emerges near 250 K, reaches its maximum intensity at T_C , and gradually

decreases at high temperatures as its spectral weight is redistributed to higher energies (Figs. 1c and 1e). Its tail extends to high energies and combines with mode 2, which partly accounts for its asymmetric lineshape. We note that the QEP in our spectra is distinct from ‘central’ peaks often observed in structural phase transitions^{41–44}; the latter typically has an extremely narrow width of the order of 1 cm^{-1} or smaller, and appears only within a few degrees about T_C . For example, the Raman spectra of LiOsO_3 show very minor change below 200 cm^{-1} across its second-order structural phase transition^{45,46}. Thus, with all the lattice degrees of freedom exhausted, the QEP can only come from electronic scattering.

In fact, electronic Raman scattering is widely observed in many strongly correlated systems^{47,48}, and in some cases serves as a sensitive indicator of an electronic phase transition. In particular, it has been shown in the context of nematic transition in iron-based superconductors that Raman response functions measure bare electronic susceptibilities without being affected by acoustic phonons^{49,50}. This allows Raman scattering to selectively probe only the electronic component of the susceptibility even when the electronic order is strongly coupled to a lattice distortion; specifically, in our case it has been pointed out in a recent theory that excitonic fluctuations can be probed in the B_{2g} channel³⁵.

In Figs. 2a and 2b, we use the electronic QEP to follow the system’s propensity toward the putative excitonic insulating phase. We present the temperature evolution in terms of Raman conductivity⁴⁷ χ''/ω in the B_{2g} channel. Provided that $\chi_{B_{2g}}$ is analytic at zero momentum and energy, integration of the Raman conductivity over all energies returns the real part of the uniform static susceptibility⁵⁰, which diverges at a thermodynamic phase transition. The QEP contribution to the conductivity increases dramatically as T_C is approached from above (Fig. 2a) and below (Fig. 2b). Figure 2c shows $\chi_{B_{2g}}$ obtained by integrating the conductivity after subtracting phonon contributions. The phonon peaks are fitted with asymmetric Fano lineshape as shown in the inset (see Supplementary Figs. 2 and 3 for the complete fitting result). The result is also in excellent agreement with that obtained using the standard coupled electron-phonon model (Supplementary Fig. 4).

The $\chi_{B_{2g}}$ shows a Curie-Weiss behavior above T_C with the Weiss temperature of $241 \pm 9\text{ K}$, extracted from linear extrapolation of the inverse susceptibility (Figs. 2c and 2d). The Weiss temperature can also be independently estimated from other quantities that are related to the correlation length. Figure 2e shows the inverse amplitude, which is expected to depend linearly on temperature near T_C , extracted by fitting to a damped harmonic oscillator lineshape. When extrapolated, they intercept the zero frequency at 244 K, giving a self-consistent quantification of the Weiss temperature. This is the temperature scale of the excitonic insulator transition that would have taken place were it not preempted by the structural phase transition at a higher temperature.

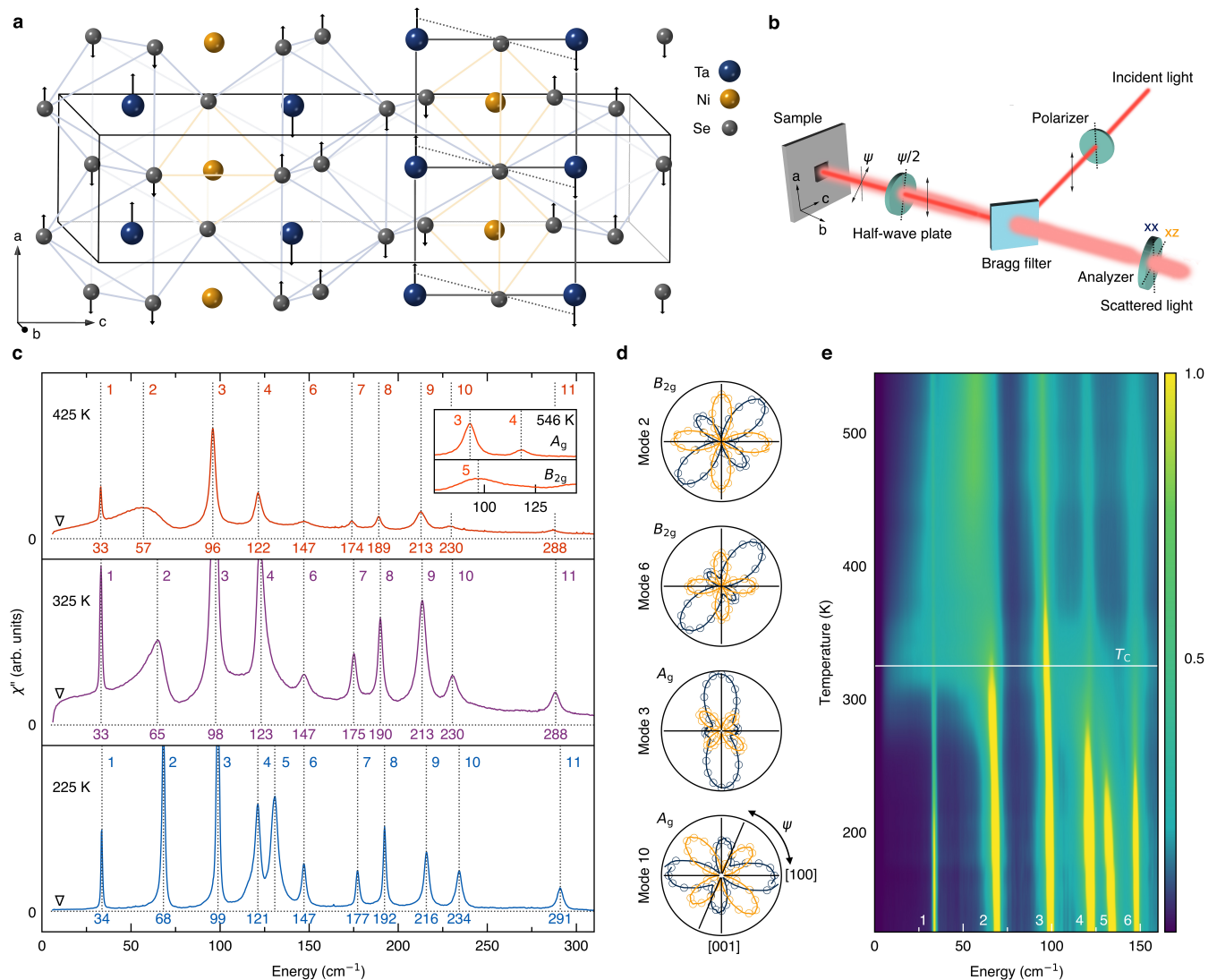


FIG. 1. **Raman-active phonon modes and a quasi-elastic peak.** **a**, Crystal structure of Ta_2NiSe_5 , overlaid with the displacement vectors ($\times 50$) in the orthorhombic-to-monoclinic transition. The black solid box shows the unit cell. The grey solid and dotted lines visualize the shearing of the quasi-one-dimensional Ta-Ni-Ta chain along the a -axis by the monoclinic distortion. **b**, Experimental configuration of the Raman measurements. **c**, Unpolarized Raman spectra at $T = 225$ K (blue), 325 K (purple), and 425 K (red). All of the eleven Raman-active modes are labeled in the order of increasing energy, and the quasi-elastic peak (QEP) is marked by an inverted triangle. The inset shows symmetry-resolved Raman spectra at $T = 546$ K. **d**, Azimuth-angle dependence of the polarization-resolved Raman scattering intensity. Ψ measures the angle between the a -axis and incident polarization, and navy (yellow) color represents the scattered-light polarization parallel (perpendicular) to the incident one. The A_g (B_{2g}) spectrum in the inset of **c** is isolated by measuring in the cross-polarization channel at $\Psi = 45^\circ$ ($\Psi = 0^\circ$). **e**, False color map of the unpolarized Raman spectra from 120 K to 550 K. $T_C = 325$ K is indicated by the white horizontal line.

The observation that the Raman susceptibility does not diverge but only is cut off at the T_C implies that it measures the electronic sub-system and not the entire system. This stems from the fact that the electron-acoustic-phonon coupling contribution to the dynamical susceptibility vanishes in the $\mathbf{q} \rightarrow 0$ limit, which is a consequence of the translation symmetry^{49,50}, or, more precisely, the fact that the symmetry generators associated with acoustic phonons commute with the conserved mo-

mentum operator of an electron⁵¹. This is analogous to the Adler's principle for a Lorentz-invariant system⁵²; a general criterion for nonrelativistic systems when the coupling between a Nambu-Goldstone boson and Landau quasiparticles vanish in the $\mathbf{q} \rightarrow 0$ limit is given in Ref. 51.

Further evidence that the excitonic instability is not driven by the structural instability is provided by the fact that excitonic fluctuations persist up to the highest measured temperature, in contrast to the softening of

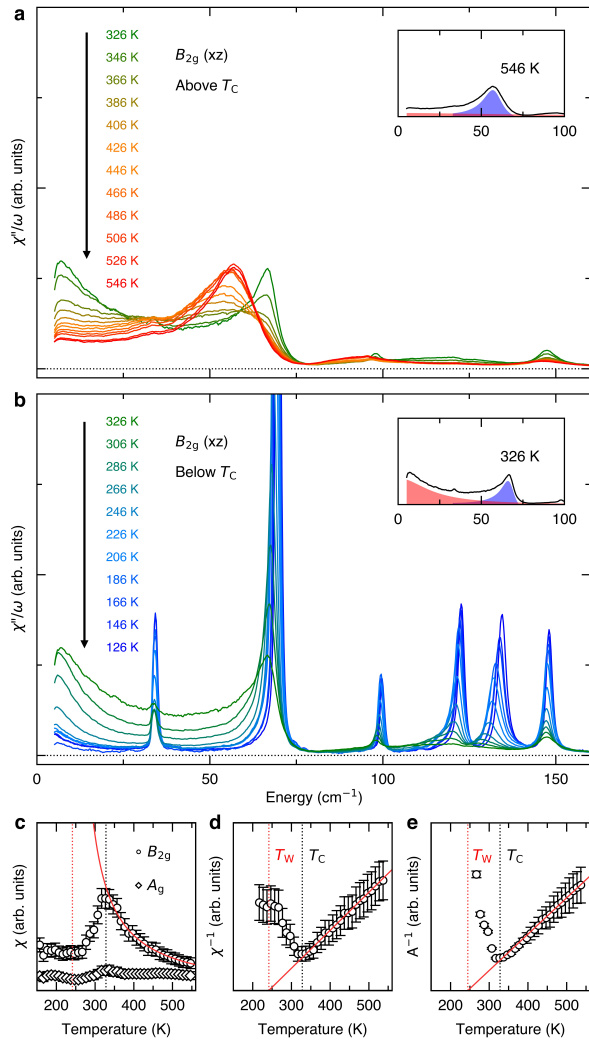


FIG. 2. Static susceptibility extracted from Raman spectra. **a, b,** Raman conductivity χ''/ω measured above and below the T_C , respectively. The insets show representative fitting of the QEP (red) and mode 2 (blue). **c,** The real part of the uniform static susceptibility obtained from integrating the Raman conductivity after subtracting the phonon contribution. The B_{2g} susceptibility (circles) follows a Curie-Weiss behaviour, whereas the A_g signal (diamonds) is nearly temperature independent. Black and red vertical lines indicate T_C and T_W , respectively. **d, e,** The temperature dependence of the inverse susceptibility and the inverse amplitude of the QEP, respectively. Red solid lines show the linear fits near the T_C . The error bars are defined by one standard deviation for the extracted values.

the B_{2g} acoustic phonon, the lowest frequency mode and hence the main driver of the structural phase transition, that significantly subsides already at 400 K³⁰.

Electron-lattice couplings, always present in all solid-state systems, have three important consequences in the present case: (i) The T_C is raised in proportion to the square of the coupling strength; (ii) The C_{55} elastic constant for the monoclinic strain (or the corresponding B_{2g}

acoustic phonon velocity) is renormalized and vanishes at the T_C , which induces a structure distortion²¹. The latter has been observed in a recent inelastic x-ray scattering study³⁰, but a more detailed temperature dependence of the elastic constant is required for a quantitative estimation of the relevant coupling parameters; (iii) The acoustic phase mode of the exciton condensate is gapped out²⁰.

The critical slowing down of the excitonic fluctuations can also be seen from their interactions and interference with phonons. Figure 3a shows the temperature evolution of the lowest-energy B_{2g} optical phonon (mode 2). As the excitonic fluctuations soften upon approaching T_C from above and sweep through mode 2, its peak amplitude, energy, width and Fano asymmetry parameter all exhibit strong anomalies (Fig. 3b). In particular, the asymmetry and the width reach a peak above the T_C as its overlap with the continuum excitations maximizes. In contrast, mode 1 remains sharp and almost symmetric, decoupled from the continuum throughout the transition. Remarkably, the asymmetric lineshape of mode 2 remains well below the T_C , implying that electronic degrees of freedom within the optical gap are not fully quenched in the insulating phase (Fig. 3c). Interestingly, mode 1 of A_g symmetry acquires small but non-zero asymmetry below T_C as a linear coupling to the continuum²⁸ becomes allowed in the monoclinic phase (Fig. 3d). The fact that the lineshape is more symmetric at high temperatures shows that the asymmetry is not simply due to thermal carriers.

Having established the electronic origin of the phase transition, we now discuss competing scenarios of the primary order being predominantly of phononic nature^{30,36,37}. A recent DFT study^{30,37} proposed that the structural phase transition is driven by an unstable B_{2g} optical phonon mode. In our data, none of the three B_{2g} optical modes shows softening upon cooling in the high-temperature phase. Rather, they become heavily damped to the extent that it is difficult to identify them in the unpolarized spectra. The center-frequency-to-width ratio for mode 2 stays below ~ 5 above the T_C , i.e. it completes only a few oscillation cycles within its lifetime. Let aside the question of softening, it barely fits the notion of a collective excitation.

Mode 5 is even more strongly damped and its weight is broadly distributed in the range 75~150 cm^{-1} close to the T_C (Fig. 4 and Supplementary Fig. 5). This mode has been predicted to be unstable in a recent DFT calculation³⁶ (see Supplementary Table 2). Below the T_C , mode 5 quickly sharpens up and its width becomes comparable to other stable modes by 225 K. In a phonon driven structural phase transition scenario, the strong damping implies a rapid anharmonic decay into a pair of B_{2g} acoustic phonons of opposite momenta⁵³, which suddenly becomes quenched by the structural phase transition. The renormalization of the B_{2g} acoustic phonon dispersion to zero velocity at $\mathbf{q}=0$ (ref. 30) reduces the phase space for anharmonic phonon-phonon scattering,

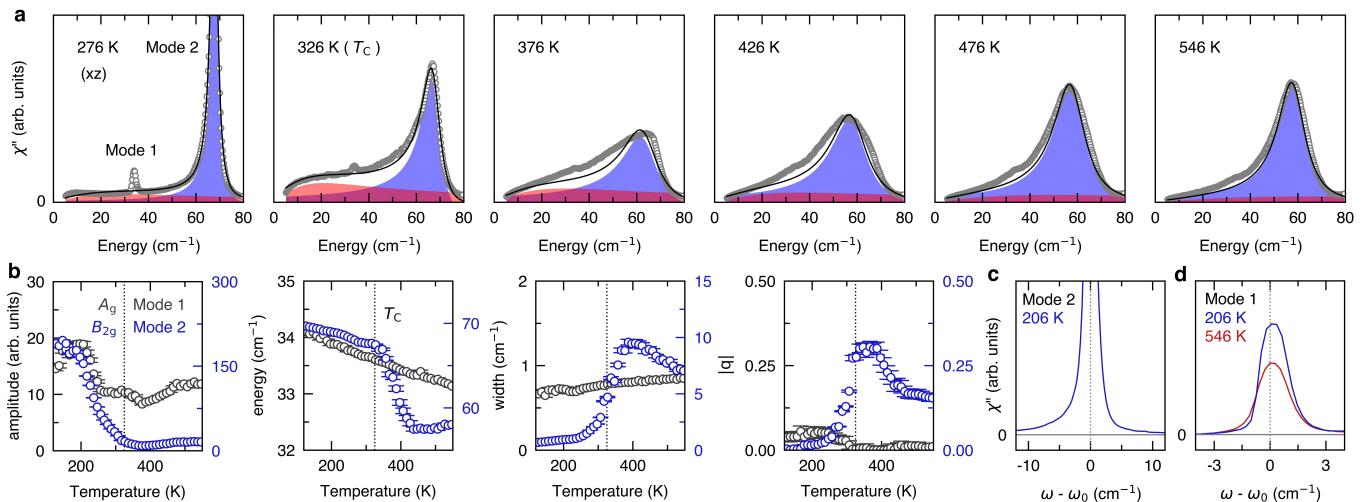


FIG. 3. **Excitonic fluctuations and phonon lineshapes.** **a**, Mode 2 (blue) fitted with the Fano lineshape and QEP (red) with the damped harmonic oscillator lineshape. **b**, Peak amplitude, energy, width, and absolute value of Fano asymmetry q extracted from the fitting, and the error bars represent the standard deviation in the fitting procedure. Black dashed line indicates T_C . **c**, Mode 2 remains asymmetric well below T_C . **d**, Mode 1 also becomes asymmetric in the low-temperature insulating phase. Black dashed lines in (c) and (d) represent the center energy of Mode 2 and Mode 1, respectively.

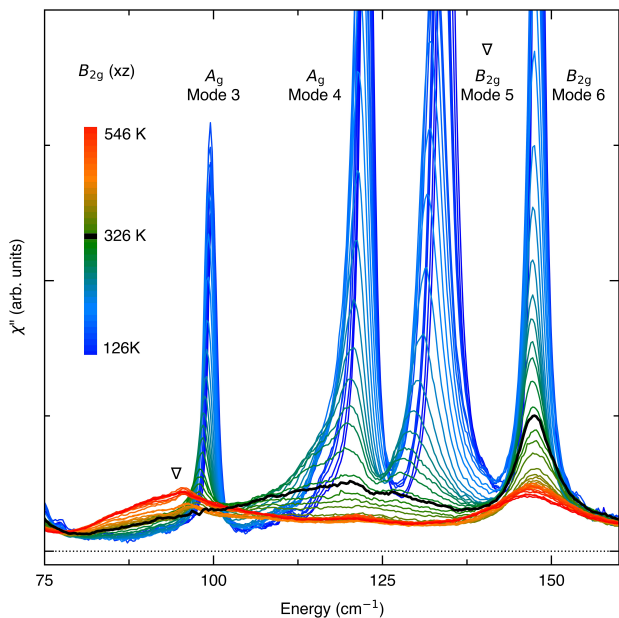


FIG. 4. **Heavily damped B_{2g} phonons.** B_{2g} Raman spectra from 126 K to 546 K. Mode 5 (inverted triangle) exhibits a large blue shift upon cooling, and is heavily damped close to the T_C (black solid line). At the highest measured temperature, all three B_{2g} modes are identified: mode 2 (Fig. 3), 5, and 6. Below T_C , A_g modes 3 and 4 also become allowed.

and thus the broadening should be minimal near the T_C , which is at odds with the experimental observation.

Instead, the exceptionally broad phonon linewidth is naturally accounted for by strong electron-phonon coupling. The phonon rapidly decays into an electron-

hole pair, and reciprocally the exciton is dressed by the phonons and acquires a heavy mass. Its spectral weight is largely lost to broad incoherent excitations that extend to high energies. We note that such exciton-phonon complexes have been observed in optical spectra^{24,27,29}. As the fluctuations slow down, excitons become trapped to lattice sites and become a static charge transfer from Ni 3d/Se 4p to Ta 5d orbitals, thereby inducing local lattice distortions which eventually trigger a structural phase transition^{18,35}. Although initially electronically driven, the eventual electronic and lattice structures are difficult to distinguish from one that results from a band hybridization driven by a structural distortion. Nevertheless, our result unambiguously shows that the phase transition is of electronic origin. Thus, the possibility to realize a pure excitonic insulator is still open, if structural distortions can be suppressed by suitable means, e.g epitaxial strain.

IV. METHODS

Sample Growth High-quality single crystals of Ta_2NiSe_5 are grown by a chemical vapor transport method. A mixture of Ta, Ni, and Se powder are sintered at 900°C for 7 days in an evacuated quartz tube. Then, the prepared Ta_2NiSe_5 powder is sealed in a quartz tube together with iodine as the transport agent and placed in a furnace with a temperature gradient between 950° and 850°. After 10 days, single crystals (a typical size of 50 μm x 1 mm x 5 mm) are obtained. Their crystallinity and stoichiometry are confirmed by x-ray diffraction and energy-dispersive spectroscopy. The crystals are further characterized by the in-plane resistivity measurements

using a Physical Properties Measurement System (Quantum Design). The transition temperature $T_C = 325$ K was identified by a clear kink in the resistivity, consistent with previous reports^{39,40}.

Raman Spectroscopy The Raman spectra are measured using a home-built Raman spectroscopy setup equipped with a 750-mm monochromator and a liquid-nitrogen-cooled CCD (Princeton Instruments) with a 633-nm He-Ne laser as the excitation source. The elastic light is removed by a set of grating-based notch filters (Optigrate, BragGrateTM Notch Filter). The home-built setup allows investigation of low-energy signals (above 5 cm^{-1}) with high energy resolution ($\sim 1 \text{ cm}^{-1}$) in various polarization channels. The samples are mounted in an open-cycle cryostat (Oxford Instruments) with temperature range from 70 K to 500 K. The measurements are conducted in a backscattering geometry where the light propagates along the b crystallographic axis. Raman response of A_g symmetry of the orthorhombic phase are

measured in $-y(xx)y$ and $-y(x'z')y$ configurations, and B_{2g} symmetry in $-y(x'x')y$ and $-y(xz)y$ configurations. We use an achromatic half-waveplate to continuously rotate the light polarization between these configurations. The laser power and the beam-spot size are 1.85 mW and $\sim 2 \mu\text{m}$, respectively, which give laser heating of 50 K according to the Stokes and anti-Stokes relation of phonons. The corrected temperature and the critical behaviors are consistent with T_C , and all the spectra are Bose-corrected. Both spectral variation in grating efficiency and silicon quantum efficiency are not accounted, which can give intensity change of $< 0.1 \%$ in total.

V. DATA AVAILABILITY

The data supporting the findings of this study are available from the corresponding author upon reasonable request.

-
- * These authors contributed equally to this work.
 † email: bjkim6@postech.ac.kr
- ¹ Zwierlein, M. W., Schunck, C. H., Schirotzek, A. & Ketterle, W. Direct observation of the superfluid phase transition in ultracold Fermi gases. *Nature* **442**, 54-58 (2006).
 - ² Zwierlein, M. W., Abo-Shaeer, J. R., Schirotzek, A., Schunck, C. H. & Ketterle, W. Vortices and superfluidity in a strongly interacting Fermi gas. *Nature* **435**, 1047-1051 (2005).
 - ³ Giovanazzi, S., Smerzi, A. & Fantoni, S. Josephson effects in dilute Bose-Einstein condensates. *Phys. Rev. Lett.* **84**, 4521 (2000).
 - ⁴ Levy, S., Lahoud, E., Shomroni, I. & Steinhauer, J. The a.c. and d.c. Josephson effects in a Bose-Einstein condensate. *Nature* **449**, 579-583 (2007).
 - ⁵ Einstein, J. P. Exciton condensation in bilayer quantum hall systems. *Annu. Rev. Condens. Matter Phys.* **5**, 159-181 (2014).
 - ⁶ Li, J. I. A., Taniguchi, T., Watanabe, K., Hone, J. & Dean, C. R. Excitonic superfluid phase in double bilayer graphene. *Nat. Phys.* **13**, 751-755 (2017).
 - ⁷ Butov, L. V. Exciton condensation in coupled quantum wells. *Solid State Commun.* **127**, 89-98 (2003).
 - ⁸ Wang, Z. et al. Evidence of high-temperature exciton condensation in two-dimensional atomic double layers. *Nature* **574**, 76-80 (2019).
 - ⁹ Keldysh, L. V. & Kopayev, Y. V. Possible instability of the semimetallic state toward coulomb interaction. *Soviet Physics Solid State, USSR* **6**, 2219-2224 (1965).
 - ¹⁰ Cloizeaux, J. D. Exciton instability and crystallographic anomalies in semiconductors. *J. Phys. Chem. Solids* **26**, 259-266 (1965).
 - ¹¹ Halperin, B. I. & Rice, T. M. Possible anomalies at a semimetal-semiconductor transition. *Rev. Mod. Phys.* **40**, 755-766 (1968).
 - ¹² Jérôme, D., Rice, T. M. & Kohn, W. Excitonic insulator. *Phys. Rev.* **158**, 462 (1967).
 - ¹³ Wakisaka, Y. et al. Excitonic insulator state in Ta_2NiSe_5 probed by photoemission spectroscopy. *Phys. Rev. Lett.* **103**, 026402 (2009).
 - ¹⁴ Wakisaka, Y. et al. Photoemission spectroscopy of Ta_2NiSe_5 . *J. Supercond. Nov. Magn.* **25**, 1231-1234 (2012).
 - ¹⁵ Kidd, T. E., Miller, T., Chou, M. Y. & Chiang, T. C. Electron-hole coupling and the charge density wave transition in TiSe_2 . *Phys. Rev. Lett.* **88**, 226402 (2002).
 - ¹⁶ Holt, M., Zschack, P., Hong, H., Chou, M. Y. & Chiang, T. C. X-ray studies of phonon softening in TiSe_2 . *Phys. Rev. Lett.* **86**, 3799 (2001).
 - ¹⁷ Kogar, A. et al. Signatures of exciton condensation in a transition metal dichalcogenide. *Science* **358**, 1314-1317 (2017).
 - ¹⁸ Kaneko, T., Toriyama, T., Konishi, T. & Ohta, Y. Orthorhombic-to-monoclinic phase transition of Ta_2NiSe_5 induced by the Bose-Einstein condensation of excitons. *Phys. Rev. B* **87**, 035121 (2013).
 - ¹⁹ Seki, K. et al. Excitonic Bose-Einstein condensation in Ta_2NiSe_5 above room temperature. *Phys. Rev. B* **90**, 155116 (2014).
 - ²⁰ Zenker, B., Fehske, H. & Beck, H. Fate of the excitonic insulator in the presence of phonons. *Phys. Rev. B* **90**, 195118 (2014).
 - ²¹ Sugimoto, K., Kaneko, T. & Ohta, Y. Microscopic quantum interference in excitonic condensation of Ta_2NiSe_5 . *Phys. Rev. B* **93**, 041105 (2016).
 - ²² Kim, S. Y. et al. Layer-confined excitonic insulating phase in ultrathin Ta_2NiSe_5 crystals. *ACS Nano* **10**, 8888-8894 (2016).
 - ²³ Lu, Y. F. et al. Zero-gap semiconductor to excitonic insulator transition in Ta_2NiSe_5 . *Nat. Commun.* **8**, 1-7 (2017).
 - ²⁴ Larkin, T. I. et al. Giant exciton fano resonance in quasi-one-dimensional Ta_2NiSe_5 . *Phys. Rev. B* **95**, 195144 (2017).
 - ²⁵ Mor, S. et al. Ultrafast electronic band gap control in an excitonic insulator. *Phys. Rev. Lett.* **119**, 086401 (2017).
 - ²⁶ Okazaki, K. et al. Photo-induced semimetallic states realised in electron-hole coupled insulators. *Nat. Commun.* **9**, 1-6 (2018).

- ²⁷ Larkin, T. I. et al. Infrared phonon spectra of quasi-one-dimensional Ta₂NiSe₅ and Ta₂NiS₅. *Phys. Rev. B* **98**, 125113 (2018).
- ²⁸ Werdehausen, D. et al. Coherent order parameter oscillations in the ground state of the excitonic insulator Ta₂NiSe₅. *Sci. Adv.* **4**, eaap8652 (2018).
- ²⁹ Sugimoto, K., Nishimoto, S., Kaneko, T. & Ohta, Y. Strong coupling nature of the excitonic insulator state in Ta₂NiSe₅. *Phys. Rev. Lett.* **120**, 247602 (2018).
- ³⁰ Nakano, A. et al. Antiferroelectric distortion with anomalous phonon softening in the excitonic insulator Ta₂NiSe₅. *Phys. Rev. B* **98**, 045139 (2018).
- ³¹ Mor, S. et al. Inhibition of the photoinduced structural phase transition in the excitonic insulator Ta₂NiSe₅. *Phys. Rev. B* **97**, 115154 (2018).
- ³² Fukutani, K. et al. Electrical tuning of the excitonic insulator ground state of Ta₂NiSe₅. *Phys. Rev. Lett.* **123**, 206401 (2019).
- ³³ Lee, J. et al. Strong interband interaction in the excitonic insulator phase of Ta₂NiSe₅. *Phys. Rev. B* **99**, 075408 (2019).
- ³⁴ Yan, J. et al. Strong electron-phonon coupling in the excitonic insulator Ta₂NiSe₅. *Inorg. Chem.* **58**, 9036-9042 (2019).
- ³⁵ Mazza, G. et al. Nature of symmetry breaking at the excitonic insulator transition: Ta₂NiSe₅. *Phys. Rev. Lett.* **124**, 197601 (2020).
- ³⁶ Subedi, A. Orthorhombic-to-monoclinic transition in Ta₂NiSe₅ due to a zone-center optical phonon instability. *Phys. Rev. Mater.* **4** 083601 (2020).
- ³⁷ Watson, M. D. et al. Band hybridization at the semimetal-semiconductor transition of Ta₂NiSe₅ enabled by mirror-symmetry breaking. *Phys. Rev. Res.* **2**, 013236 (2020).
- ³⁸ Tang, T. et al. Non-coulomb strong electron-hole binding in Ta₂NiSe₅ revealed by time- and angle-resolved photoemission spectroscopy. *Phys. Rev. B* **101**, 235148 (2020).
- ³⁹ Sunshine, S. A. & Ibers, J. A. Structure and physical properties of the new layered ternary chalcogenides Ta₂NiS₅ and Ta₂NiSe₅. *Inorg. Chem.* **24**, 3611-3614 (1985).
- ⁴⁰ Di Salvo, F. J. et al. Physical and structural properties of the new layered compounds Ta₂NiS₅ and Ta₂NiSe₅. *J. Less-Common Met.* **116**, 51-61 (1986).
- ⁴¹ Axe, J. D. & Shirane, G. Inelastic-neutron-scattering study of acoustic phonons in Nb₃Sn. *Phys. Rev. B* **8**, 1965-1977 (1973).
- ⁴² Steiner, M., Kakurai, K. & Knob, W. Neutron inelastic scattering study of transverse spin fluctuations in CsNiF₃. *Solid State Commun.* **41**, 329-332 (1982).
- ⁴³ Sato, M., Fujishita, H., Sato, S. & Hoshino, S. Neutron inelastic scattering and x-ray structural study of the charge-density-wave state in K_{0.3}MoO₃. *J. Phys. C Solid State Phys.* **18**, 2603-2614 (1985).
- ⁴⁴ Lockwood, D., Arthur, J., Taylor, W. & Hosea, T. Observation of a central peak in lead germanite by light scattering. *Solid State Commun.* **20**, 703-707 (1976).
- ⁴⁵ Shi, Y. et al. A ferroelectric-like structural transition in a metal. *Nat. Mater.* **12**, 1024-1027 (2013).
- ⁴⁶ Jin, F. et al. Raman interrogation of the ferroelectric phase transition in polar metal LiOsO₃. *Proc. Natl. Acad. Sci. U.S.A.* **116**, 20322-20327 (2019).
- ⁴⁷ Shastry, B. S. & Shraiman, B. I. Theory of Raman scattering in Mott-Hubbard systems. *Phys. Rev. Lett.* **65**, 1068-1071 (1990).
- ⁴⁸ Devereaux, T. P. & Hackl, R. Inelastic light scattering from correlated electrons. *Rev. Mod. Phys.* **79**, 175-233 (2007).
- ⁴⁹ Massat, P. et al. Charge-induced nematicity in FeSe. *Proc. Natl. Acad. Sci. U.S.A.* **113**, 9177-9181 (2016).
- ⁵⁰ Gallais, Y. & Paul, I. Charge nematicity and electronic Raman scattering in iron-based superconductors. *C. R. Phys.* **17**, 113-139 (2016).
- ⁵¹ Watanabe, H. & Vishwanath, A. Criterion for stability of Goldstone modes and Fermi liquid behavior in a metal with broken symmetry. *Proc. Natl. Acad. Sci. U.S.A.* **111**, 16314-16318 (2014).
- ⁵² Adler, S. L. Consistency conditions on the strong interactions implied by a partially conserved axial-vector current. *Phys. Rev.* **137**, B1022-B1033 (1965).
- ⁵³ Klemens, P. G. Anharmonic decay of optical phonons. *Phys. Rev.* **148**, 845-848 (1966).
- ⁵⁴ Andrich, P. et al. Imaging the coherent propagation of collective modes in the excitonic insulator candidate Ta₂NiSe₅ at room temperature. Preprint at <http://arxiv.org/abs/2003.10799> (2020).
- ⁵⁵ Baldini, E. et al. The spontaneous symmetry breaking in Ta₂NiSe₅ is structural in nature. Preprint at <http://arxiv.org/abs/2007.02909> (2020).
- ⁵⁶ Kim, M.-J. et al. Phononic soft mode behavior and a strong electronic background across the structural phase transition in the excitonic insulator Ta₂NiSe₅. *Phys. Rev. Res.* **2**, 042039(R) (2020).
- ⁵⁷ Volkov, P. A. et al. Critical charge fluctuations and quantum coherent state in excitonic insulator Ta₂NiSe₅. Preprint at <http://arxiv.org/abs/2007.07344> (2020).

VI. ACKNOWLEDGMENTS

We thank A. Subedi, G. Y. Cho, E.-G. Moon, K.-Y. Choi, H. W. Yeom, and K.-S. Kim for useful discussions. This project is supported by IBS-R014-A2 and National Research Foundation (NRF) of Korea through the SRC (no. 2018R1A5A6075964).

Supplementary Information

Direct observation of excitonic instability in Ta_2NiSe_5

Kwangrae Kim,^{1,2,*} Hoon Kim,^{1,2,*} Jonghwan Kim,^{2,3} Changil Kwon,^{1,2} Jun Sung Kim,^{1,2}
and B. J. Kim^{1,2,†}

¹Department of Physics, Pohang University of Science and Technology, Pohang 37673, South Korea

²Center for Artificial Low Dimensional Electronic Systems, Institute for Basic Science (IBS), 77 Cheongam-Ro, Pohang 37673, South Korea

³Department of Materials Science and Engineering, Pohang University of Science and Technology, Pohang 37673, Republic of Korea

*These authors contributed equally to this work.

†Corresponding author (bjkim6@postech.ac.kr)

Supplementary Note 1: AZIMUTH ANGLE DEPENDENCE OF THE RAMAN-ACTIVE PHONON MODES

In the orthorhombic $Cmcm$ phase, the Raman tensors have the following forms:

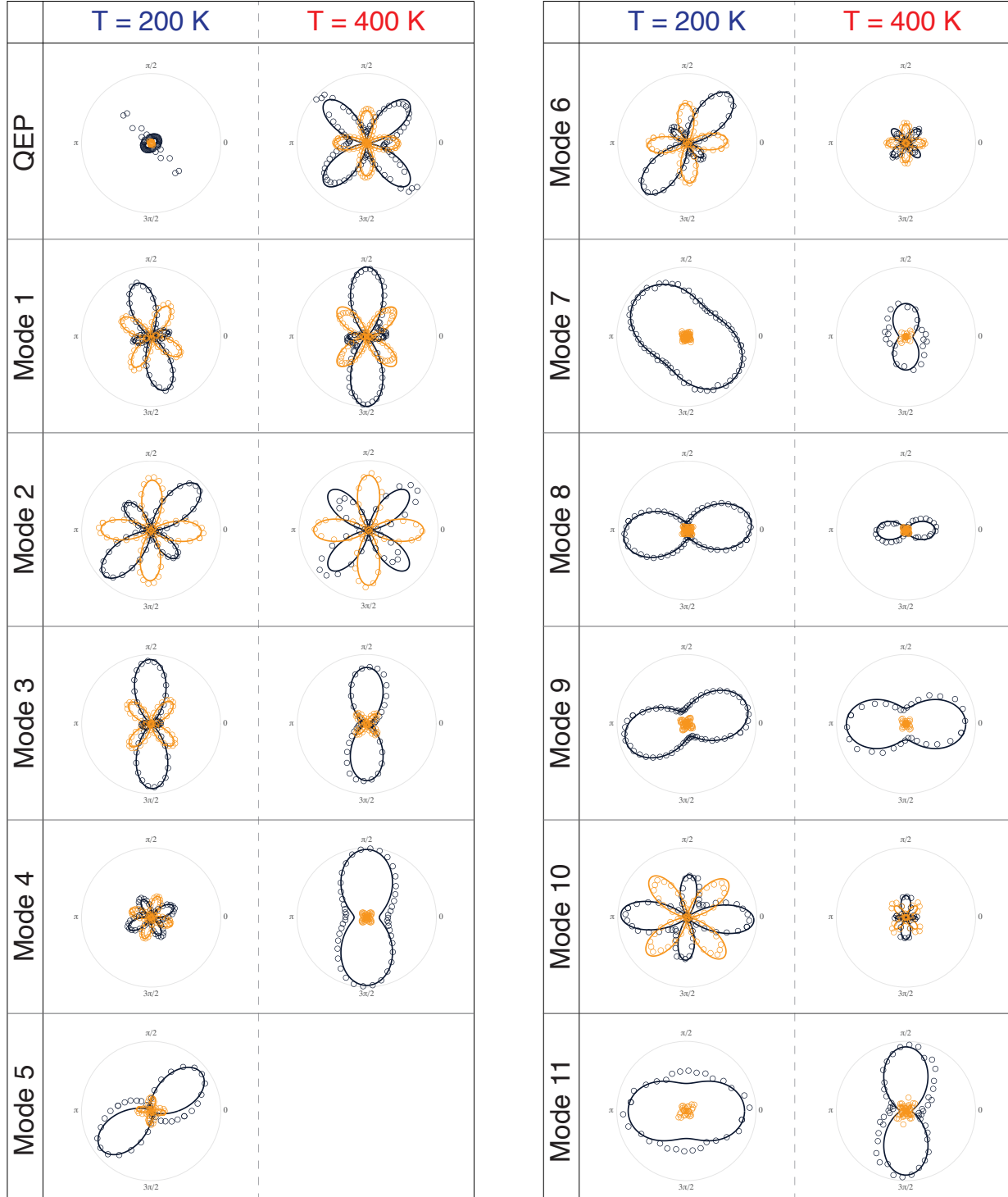
$$\hat{R}(A_g) = \begin{pmatrix} c_1 & & \\ & c_2 & \\ & & c_3 \end{pmatrix}, \quad \hat{R}(B_{2g}) = \begin{pmatrix} & c_4 & \\ & & \\ c_4 & & \end{pmatrix}, \quad (1)$$

where c_1 , c_2 , c_3 , and c_4 are non-zero elements. Further, c_2 is identically zero in our $-y(xz)y$ configuration. For cross polarization at $\Psi=0^\circ$ (yellow patterns in Supplementary Fig. 1), A_g (B_{2g}) Raman intensity vanishes (is maximized), because only off-diagonal components contribute to the intensity. Likewise, A_g Raman intensity is maximized at $\Psi=45^\circ$ while B_{2g} intensity is completely suppressed. This allows a clear separation of A_g and B_{2g} spectra as shown in the inset of Fig. 1c. Thus, mode 2, 5, 6 and QEP are unambiguously assigned as B_{2g} and the remaining eight modes as A_g . Although the azimuth profile of mode 5 at high temperature is not clearly of B_{2g} type due to its overlap with mode 3 and mode 4 of A_g symmetry, mode 5 is clearly identified as a well-defined peak in the B_{2g} spectrum shown in the inset of Fig. 1c.

Below T_C , A_g and B_{2g} are no longer distinct and the Raman tensor acquires the form:

$$\hat{R}(A_g) = \begin{pmatrix} c_1 & c_4 \\ & c_2 \\ c_4 & c_3 \end{pmatrix}. \quad (2)$$

The mixing between A_g and B_{2g} modes leads to intensity extrema deviating from the high-symmetry crystallographic directions (see, e.g., mode 1, 4, 7, and 9 in Supplementary Fig. 1). In Supplementary Table 1, we summarize the fitting results of the polarization dependence of all the modes, using Supplementary Eq. (1) and (2) at 200 K and 400 K, respectively.

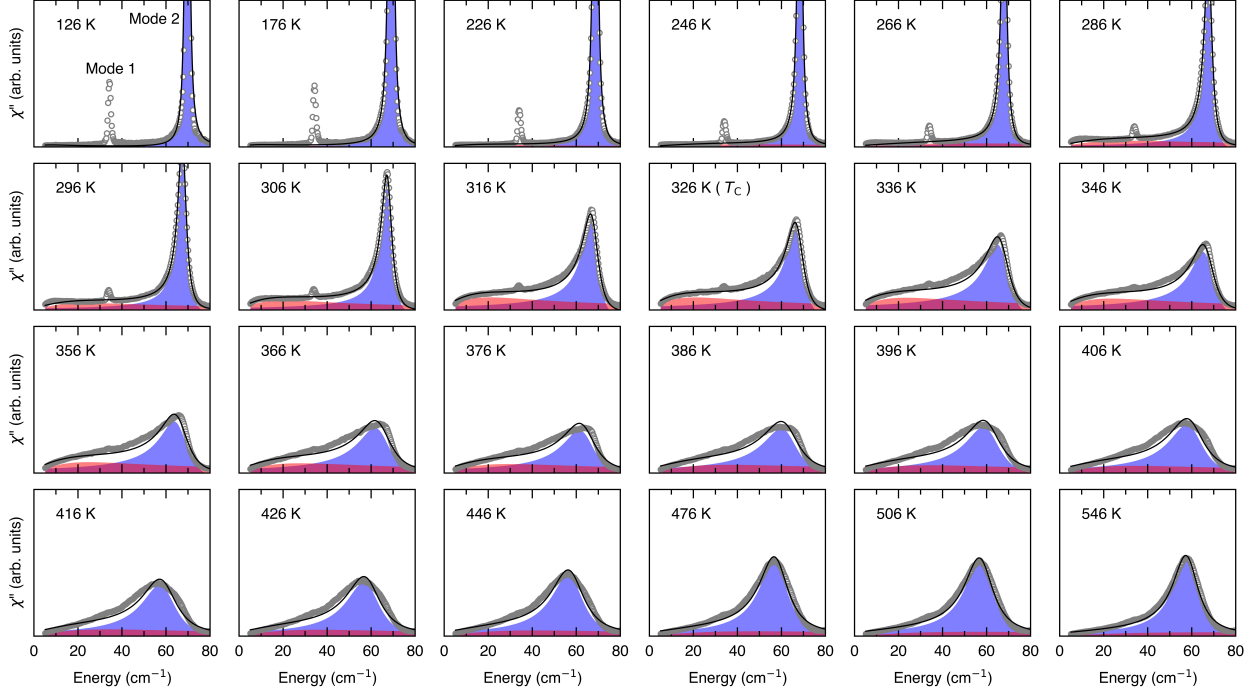


Supplementary Figure 1 | Azimuth-angle dependence of the the quasi-elastic peak and the phonon modes. Polar plot of Raman intensity as a function of the angle between the incident polarization and the a -axis below and above the T_C . Navy and yellow colors represent the parallel- and cross-polarization configurations, respectively. Solid lines are fitting results shown in Supplementary Table 1.

Mode	IR	Orthorhombic (<i>Cmcm</i>) at 400 K			Monoclinic (<i>C2/c</i>) at 200 K		
		c_1	c_3	c_4	c_1	c_3	c_4
QEP	B_{2g}			1			
1	A_g	0.34	-0.66		0.27	-0.51	0.22
2	B_{2g}			1	0.15	0.07	0.78
3	A_g	-0.02	0.98		0.26	-0.71	0.02
4	A_g	0.30	0.70		-0.34	0.28	-0.39
5	B_{2g}				0.44	0.26	0.31
6	B_{2g}			1	0.10	0.26	0.64
7	A_g	0.32	0.68		0.48	0.45	-0.07
8	A_g	0.87	0.13		0.70	0.25	0.05
9	A_g	0.66	0.34		0.60	0.31	0.09
10	A_g	-0.41	0.59		-0.53	0.43	0.04
11	A_g	0.24	0.76		0.59	0.41	0

Supplementary Table 1 | Raman tensor elements. Fitting of the polarization dependence of the Raman modes, using the tensors given in Supplementary Eq. (1) and (2). The results are overlaid with the data points in Supplementary Fig. 1. The coefficients are normalized in such a way that $\|c_1\| + \|c_3\| + \|c_4\| = 1$.

Supplementary Note 2: FITTING RESULTS USING TWO DIFFERENT MODELS



Supplementary Figure 2 | Fitting result using the Fano lineshape (blue) and the damped harmonic oscillator lineshape (red). All measured spectra at temperatures between 280 K and 420 K are shown.

In the main text, we analyze the spectra below 100 cm^{-1} using an independent electron-phonon model (Model 1) where we fit the QEP using damped harmonic oscillator lineshape and mode 2 with Fano lineshape, expressed in Supplementary Eq. (3) and (4), respectively. The damped harmonic oscillator (or the Drude-Lorentz) is a typical model for electronically scattered Raman signals, and the Fano lineshape is generally used for phonon modes that couple to a continuum, where q determines their asymmetry, and thus their coupling strengths to the continuum. The lineshapes are expressed as

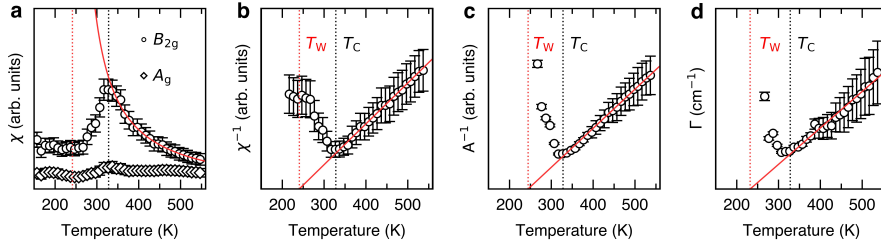
$$\chi''_{\text{electron}}(\omega) = \frac{A_{\text{el}}\Gamma_{\text{el}}\omega}{\Gamma_{\text{el}}^2 + \omega^2}, \quad (3)$$

$$\chi''_{\text{phonon}}(\omega) = \frac{A_{\text{ph}}(1 + q\epsilon)^2}{1 + \epsilon^2}, \quad \epsilon = \frac{\omega - \omega_{\text{ph}}}{\Gamma_{\text{ph}}}, \quad (4)$$

where χ''_{electron} and χ''_{phonon} is bose-corrected Raman intensity of QEP and optical phonon mode 2. A_{el} , Γ_{el} , A_{ph} , ω_{ph} , Γ_{ph} , and q indicate the amplitude, width of QEP, amplitude,

energy, width of mode 2, and the asymmetry of mode 2 respectively.

All measured spectra are fitted with the six adjustable parameters, and the result is shown in Supplementary Fig. 2. As shown in Fig. 2 and Supplementary Fig. 3, the extracted electronic susceptibility follows Curie-Weiss behavior above T_C with the Weiss temperature around 241 K. The inverse of QEP amplitude from fit shows a linear behavior above T_C , intercepting the zero at 244 K when extrapolated. In addition to parameters in Fig. 2, the width of QEP also increases linearly above T_C with an intercept at 235 K (Supplementary Fig. 3).



Supplementary Figure 3 | Fitting parameters for QEP. **a**, Electronic susceptibility in A_g (diamond) and B_{2g} (circle) channel. **b**, the inverse of B_{2g} electronic susceptibility. **c**, the inverse of QEP amplitude. **d**, the width of QEP. Error bars indicate the standard deviation from the fitting procedure.

In the below, we use a different model (Model 2), which takes into account the coupling between the QEP and mode 2, to fit the same spectra [1, 2]. In this model, the bare electron and the phonon Green functions, expressed as (with ω_{ph} and Γ_{ph} denoting energy and width of the phonon mode 2, respectively, and Γ_{el} the width of the QEP)

$$G_{\text{electron}}(\omega) = \frac{1}{\Gamma_{\text{el}} - i\omega}, \quad (5)$$

$$G_{\text{phonon}}(\omega) = -\frac{1}{\omega - \omega_{\text{ph}} + i\Gamma_{\text{ph}}} + \frac{1}{\omega + \omega_{\text{ph}} + i\Gamma_{\text{ph}}}, \quad (6)$$

are coupled by v to give the total Green function

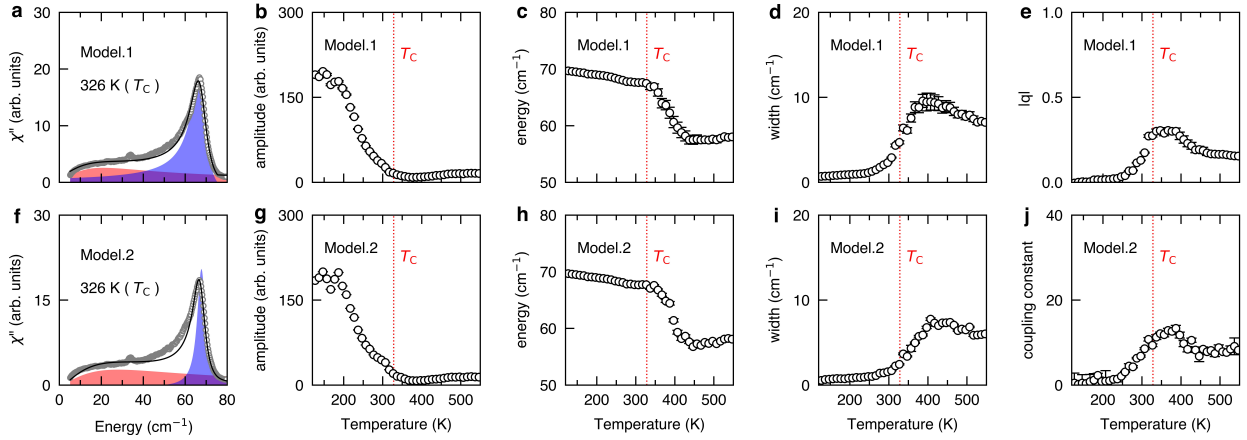
$$G(\omega) = \begin{bmatrix} G_{\text{electron}}^{-1}(\omega) & v \\ v & G_{\text{phonon}}^{-1}(\omega) \end{bmatrix}^{-1}, \quad (7)$$

which is related to the Raman susceptibility via

$$\chi''(\omega) = \text{Im } TGT, \quad (8)$$

where $T = [t_{\text{el}} t_{\text{ph}}]$ is the amplitude for Raman light scattering process.

The fit result using this model is compared to the previous one (Model 1) in Supplementary Fig. 4. The amplitude, energy, and width of mode 2 are common for the two models, and thus can be directly compared to each other. We find an excellent agreement between the two sets of parameters. Although the q -asymmetry parameter in Model 1 and the coupling constant v in Model 2 have different physical meanings, they have similar temperature dependencies, reflecting the phonon anomaly that becomes pronounced around 400 K upon cooling.



Supplementary Figure 4 | Fitting results for mode 2 with different fitting methods.

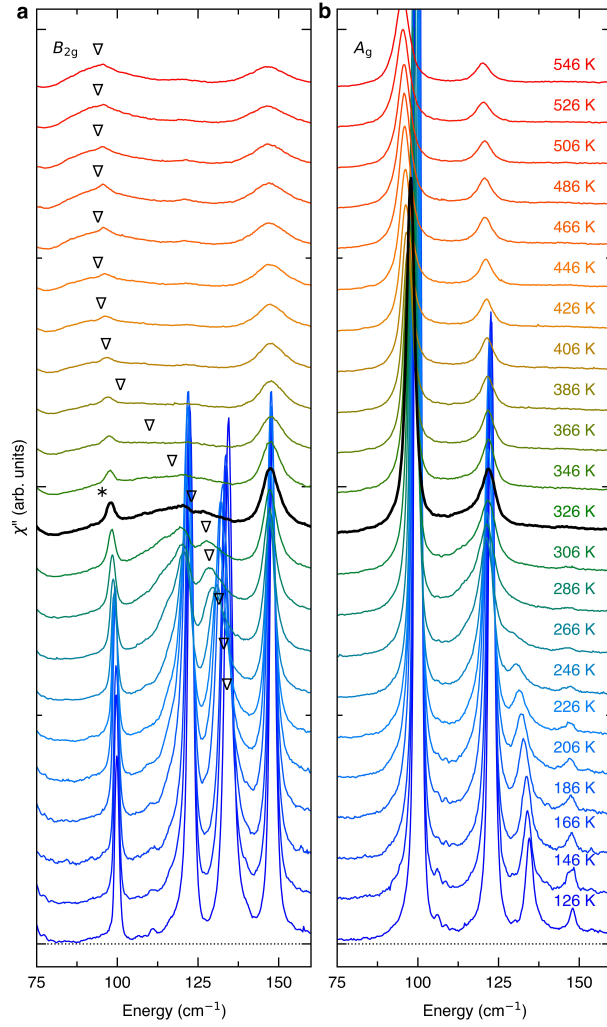
a, QEP (red) fitted with the damped harmonic oscillator lineshape, and mode 2 (blue) with the Fano lineshape, respectively. **b-e**, amplitude, energy, width, and asymmetry of mode 2 from fitting method 1. **f**, QEP and mode 2 fitted with fitting method 2. Bare electronic feature (red) and mode 2 (blue) without electron-phonon coupling are shown. **g-j**, amplitude, energy, width, and asymmetry of mode 2 from fitting method 2.

**Supplementary Note 3: IDENTIFICATION OF THE UNSTABLE OPTICAL MODE
IN THE DENSITY FUNCTIONAL CALCULATION**

Mode	IR	Orthorhombic ($Cmcm$)		Monoclinic ($C2/c$)	
		Exp. at 546 K (cm^{-1})	Calc. (cm^{-1})	Exp. at 100 K (cm^{-1})	Calc. (cm^{-1})
1	A_g	33	32.272	34	32.448
2	B_{2g}	57	74.755	69	59.704
3	A_g	95	94.880	99	95.020
4	A_g	120	120.515	122	120.569
5	B_{2g}	94		134	
6	B_{2g}	146	149.189	148	145.162
7	A_g	174	169.927	178	170.196
8	A_g	189	183.266	194	184.076
9	A_g	213	200.463	217	203.635
10	A_g	228	220.940	236	222.760
11	A_g	287	280.743	293	281.137

Supplementary Table 2 | Raman active phonon modes. Comparison between the calculated [3] and the measured mode energies. The IRs listed are based on the high-temperature phase. All of the phonon modes reduce to A_g IR in the monoclinic phase.

We identify the unstable optical mode in the DFT calculation to be the mode 5 in our data by comparing the measured phonon energies to the ones from the DFT calculation [3]. Their energies are in overall good agreement with each other except for the mode 5, which therefore is the one that has a negative energy in the DFT calculation. As shown in Fig. 4 and Supplementary Fig. 5, this mode does not soften to zero frequency, but hardens as the acoustic mode freezes.



Supplementary Figure 5 | Vertically stacked Raman spectra. **a**, B_{2g} Raman spectra measured in $-y(xz)y$. **b**, A_g in $-y(xx)y$. Black solid line indicates T_C , and the leakage of A_g mode 3 is marked by an asterisk. Mode 5 (inverted triangle) is heavily damped at T_C , but never softens to zero energy.

-
- [1] Klein, M. V. "Electronic Raman Scattering" in *Light Scattering in Solids I* **8**, 147-202 (Springer-Verlag Berlin, 1983)
- [2] Volkov, P. A. et al. Critical charge fluctuations and quantum coherent state in excitonic insulator Ta₂NiSe₅. Preprint at <http://arxiv.org/abs/2007.07344> (2020).
- [3] Subedi, A. Orthorhombic-to-monoclinic transition in Ta₂NiSe₅ due to a zone-center optical phonon instability. *Phys. Rev. Mater.* **4**, 083601 (2020).